



Ionic transport in $(\text{La,Sr})\text{CoO}_{3-\delta}$ ceramics

E. V. Tsipis¹ · E. N. Naumovich^{2,3} · M. V. Patrakeev⁴ · A. A. Yaremchenko⁵ · A. V. Kovalevsky⁵ · J. C. Waerenborgh⁶ · V. V. Kharton¹

Received: 27 June 2021 / Revised: 9 August 2021 / Accepted: 9 August 2021 / Published online: 28 October 2021
© The Author(s), under exclusive licence to Springer-Verlag GmbH Germany, part of Springer Nature 2021

Abstract

Increasing Sr^{2+} concentration and the creation of A-site deficiency in $\text{La}_{1-x-y}\text{Sr}_x\text{CoO}_{3-\delta}$ ($x=0.3-0.7$, $y=0-0.05$) increase oxygen ionic conductivity, oxygen permeability of the dense ceramic membranes, and surface exchange limitations, in correlation with the oxygen nonstoichiometry variations. Regression analysis of the experimental data on oxygen deficiency and steady-state oxygen permeation fluxes demonstrated an important role of the defect association processes, namely, clustering of the oxygen vacancies and Co^{2+} . The X-ray diffraction and Mössbauer spectroscopy studies of model ^{57}Fe -doped composition, $\text{La}_{0.3}\text{Sr}_{0.7}\text{Co}_{0.99}\text{Fe}_{0.01}\text{O}_{3-\delta}$, confirmed that the ordering processes occur on reduction. In the case of $\text{La}_{0.5}\text{Sr}_{0.5}\text{CoO}_{3-\delta}$ when oxygen transport limitations by bulk ionic conduction and surface exchange are comparable, the exchange limitations are located essentially at the membrane permeate-side surface. Reducing $p(\text{O}_2)$ and temperature leads to greater surface limitations. The chemically induced lattice expansion increases with increasing both x and y in $\text{La}_{1-x-y}\text{Sr}_x\text{CoO}_{3-\delta}$, as well as with increasing temperature. The apparent thermal expansion coefficients calculated from the dilatometric data in air vary from $(16-17) \times 10^{-6} \text{ K}^{-1}$ at 300–950 K up to $(28-31) \times 10^{-6} \text{ K}^{-1}$ at 750–1370 K.

Introduction

Oxide materials based on lanthanum-strontium cobaltites with ABO_3 perovskite-type structure, $(\text{La,Sr})\text{CoO}_{3-\delta}$, are promising for numerous electrochemical and catalytic applications, including dense ceramic membranes for gas separation, air electrodes of intermediate-temperature solid oxide fuel cells and electrolysis cells (SOFCs/SOECs), and

catalytic afterburners. Moreover, over the past 5–7 years, the $\text{La}_{1-x}\text{Sr}_x\text{CoO}_{3-\delta}$ solid solutions with $x \approx 0.4$ have become state-of-the-art air electrodes used in the commercial SOFC/SOEC cells operating at temperatures $\leq 1073 \text{ K}$ [1–3]. These phases possess a very high level of mixed oxygen-ionic and electronic conductivity, fast surface oxygen exchange kinetics, and high catalytic and electrocatalytic activity for various oxidation–reduction processes ([4–20] and references cited). The functional properties of cobaltites are governed by the oxidation states of B-site cations, the delocalization degree of electronic charge carriers, the level of oxygen deficiency, the presence or absence of short- and long-range ordering processes, and spin transitions of cobalt ions.

The gradual incorporation of Sr^{2+} cations into the lattice of $\text{La}_{1-x}\text{Sr}_x\text{CoO}_{3-\delta}$ leads first to an increase in the oxidation state of cobalt cations and then to the progressive formation of oxygen vacancies. Accordingly, the total electrical conductivity, dominated in air by p-type electronic transport, exhibits a maximum at $x \approx 0.3-0.4$. The partial ionic conductivity increases with strontium content up to $x \approx 0.7$ and decreases on further doping due to the ordering processes in the oxygen sublattice and phase separation [4, 10–12, 21]. The effect of A-site deficiency on the partial conductivities is studied insufficiently. Considering essentially itinerant nature of p-type electronic charge carriers and

✉ V. V. Kharton
kharton@issp.ac.ru

¹ Osipyan Institute of Solid State Physics RAS, 142432, Chernogolovka, Moscow District, Russia

² Institute of Power Engineering, Mory 8, 01-330 Warsaw, Poland

³ Center for Hydrogen Technologies (CTH2), Institute of Power Engineering, Augustowka 36, 02-981 Warsaw, Poland

⁴ Institute of Solid State Chemistry, Ural Branch of RAS, 91 Pervomayskaya Str, Ekaterinburg 620990, Russia

⁵ CICECO, Aveiro Institute of Materials, Department of Materials and Ceramic Engineering, University of Aveiro, 3810-193 Aveiro, Portugal

⁶ Centro de Ciências e Tecnologias Nucleares, DECN, Instituto Superior Técnico, Universidade de Lisboa, 2695-066 Bobadela LRS, Portugal

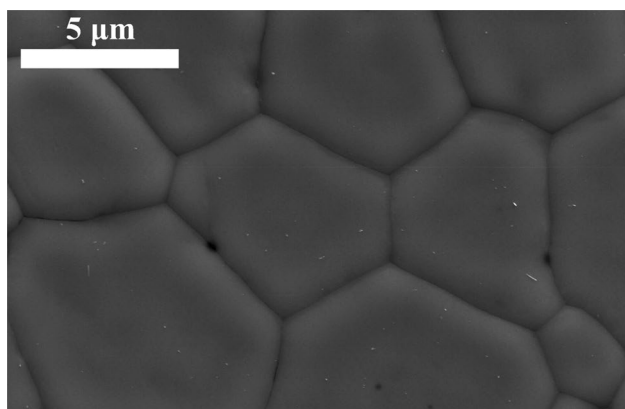


Fig. 1 SEM micrograph of polished and thermally etched $\text{La}_{0.5}\text{Sr}_{0.5}\text{CoO}_{3-\delta}$ ceramics

non-idealities in the oxygen sublattice, the behavior of oxygen nonstoichiometry and concentrations of mobile charge carriers in $(\text{La},\text{Sr})\text{CoO}_{3-\delta}$ may obey neither simplified point-defect nor rigid-band models, commonly used in the literature. The oxygen permeability of dense $\text{La}_{0.3}\text{Sr}_{0.7}\text{CoO}_{3-\delta}$ membranes was reported to be controlled mainly by bulk diffusion across the membrane in the range of thickness 0.57–2.15 mm at 1023–1373 K [13]. Preliminary data [14] suggest that the oxygen permeation through 1.0–1.4-mm-thick $\text{La}_{1-x}\text{Sr}_x\text{CoO}_{3-\delta}$ membranes is affected by the surface oxygen exchange kinetics at $x \geq 0.5$. However, revealing the role and location of surface limitations requires additional studies.

This work continuing our research on lanthanum-strontium cobaltites [9, 14–16] is focused on the comprehensive characterization of $\text{La}_{1-x-y}\text{Sr}_x\text{CoO}_{3-\delta}$ ($x = 0.3\text{--}0.7$, $y = 0\text{--}0.05$), including the local structural features,

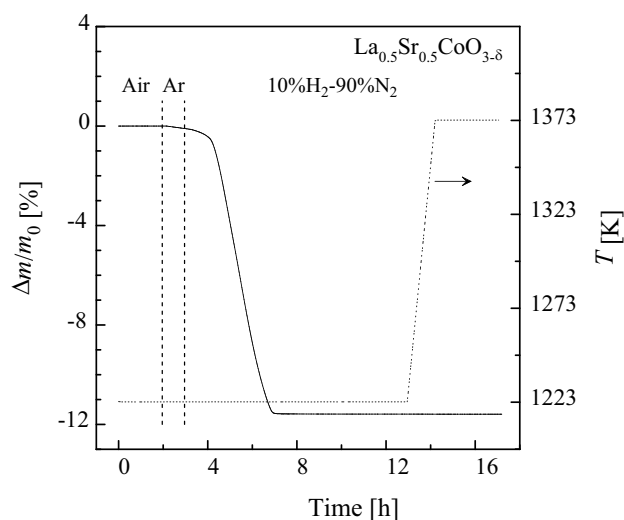


Fig. 2 Example of thermogravimetric data illustrating the determination of total oxygen content in $\text{La}_{0.5}\text{Sr}_{0.5}\text{CoO}_{3-\delta}$ powder at 1223 K and atmospheric oxygen pressure

thermomechanical properties, and oxygen ionic and electronic transport. A special attention is given to the analysis of steady-state oxygen permeation fluxes through the dense ceramic membranes. The equilibrium $p(\text{O}_2)$ - T - δ diagrams of $\text{La}_{1-x}\text{Sr}_x\text{CoO}_{3-\delta}$ ($x = 0.3\text{--}0.7$) were analyzed previously [14] by a model combining the rigid-band approach for delocalized holes and the pair-cluster formation reaction involving oxygen vacancies and Co^{2+} cations, neglecting coulombic repulsion between the positively charged vacancies. The resultant relationships between the oxygen chemical potential and mobile vacancy concentration are used in this work for numerical regression analysis of the steady-state oxygen permeation through the cobaltite membranes.

Table 1 Properties of the $\text{La}_{1-x-y}\text{Sr}_x\text{CoO}_{3-\delta}$ ceramics in air

Composition (space group)	Unit cell parameters	Relative density, %	Average linear thermal expansion coefficients		Activation energy for oxygen permeability**	
			T , K	$\text{TEC} \times 10^6$, K^{-1}	T , K	E_a , kJ/mol
$\text{La}_{0.70}\text{Sr}_{0.30}\text{CoO}_{3-\delta}$ (S.G. $R\bar{3}c$)	$a = 5.4039(2)$ Å $\alpha = 60.434(2)^\circ$	95	350–950 1070–1370	17.15 ± 0.01 27.55 ± 0.08	1123–1223	153 ± 17
$\text{La}_{0.65}\text{Sr}_{0.30}\text{CoO}_{3-\delta}$ (S.G. $R\bar{3}c$) *	$a = 5.4094(2)$ Å $\alpha = 60.271(2)^\circ$	94	350–850 970–1170	16.35 ± 0.02 28.71 ± 0.04	1073–1223	102 ± 10
$\text{La}_{0.55}\text{Sr}_{0.40}\text{CoO}_{3-\delta}$ (S.G. $Pm\bar{3}m$) *	$a = 3.844(3)$ Å	99	350–850 970–1170	16.46 ± 0.02 30.89 ± 0.09	1123–1223	101 ± 41
$\text{La}_{0.50}\text{Sr}_{0.50}\text{CoO}_{3-\delta}$ (S.G. $R\bar{3}c$)	$a = 5.4243(2)$ Å $\alpha = 59.871(3)^\circ$	93	350–850 970–1370	17.04 ± 0.03 31.17 ± 0.06	1123–1223	94.4 ± 0.2
$\text{La}_{0.30}\text{Sr}_{0.70}\text{CoO}_{3-\delta}$ (S.G. $Pm\bar{3}m$)	$a = 3.836(4)$ Å	93	300–750 750–1100	19.6 ± 0.5 28.8 ± 0.5	1073–1223	69 ± 9

*Contained < 2 wt% CoO

**Data refer to 1.0-mm-thick membrane under the oxygen partial pressure gradient of 0.021/0.21 atm

Experimental

Experimental procedures used for the synthesis and processing of $\text{La}_{1-x}\text{Sr}_x\text{CoO}_{3-\delta}$ ($x=0.3, 0.5$ and 0.7) were reported elsewhere [14]. The A-site-deficient $\text{La}_{0.95-x}\text{Sr}_x\text{CoO}_{3-\delta}$ ($x=0.3, 0.4$ and 0.5) and samples doped with 1 mol% ^{57}Fe isotope, $\text{La}_{1-x}\text{Sr}_x\text{Co}_{0.99}\text{Fe}_{0.01}\text{O}_{3-\delta}$ ($x=0.3, 0.5$ and 0.7), for the Mössbauer spectroscopy (MS) studies, were prepared by the glycine-nitrate synthesis route in a similar way. The dense gas-tight ceramics were sintered in air at 1520–1650 K for 2 h. The density of ceramics was no less than 93% of their theoretical density calculated from the X-ray diffraction (XRD) results (Table 1). Figure 1 presents a scanning electron microscopy (SEM) image reflecting microstructure typical for the sintered ceramics. The average grain size was

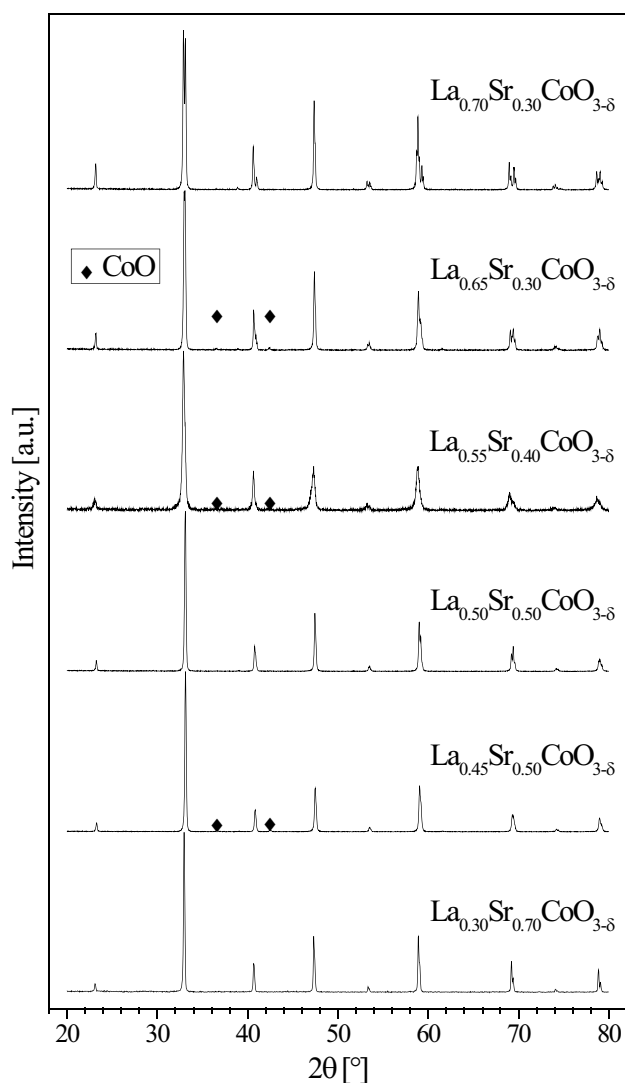


Fig. 3 X-ray diffraction patterns of powdered $\text{La}_{1-x}\text{Sr}_x\text{CoO}_{3-\delta}$ ceramics sintered in air

similar for all materials, varying in the range 2–10 μm . The powdered samples used for XRD, thermogravimetric analysis (TGA) and Mössbauer spectroscopy were obtained by grinding of the sintered ceramics.

The samples for Mössbauer spectroscopy were either annealed in air and then slowly cooled, or annealed in flowing argon at 973–1223 K for 10 h and quenched in liquid nitrogen. The Mössbauer spectra were collected at 290 and 4 K (with the sample immersed in liquid He) on a conventional transmission constant-acceleration spectrometer with a ^{57}Co (Rh) source as described elsewhere [22–25] and analyzed using

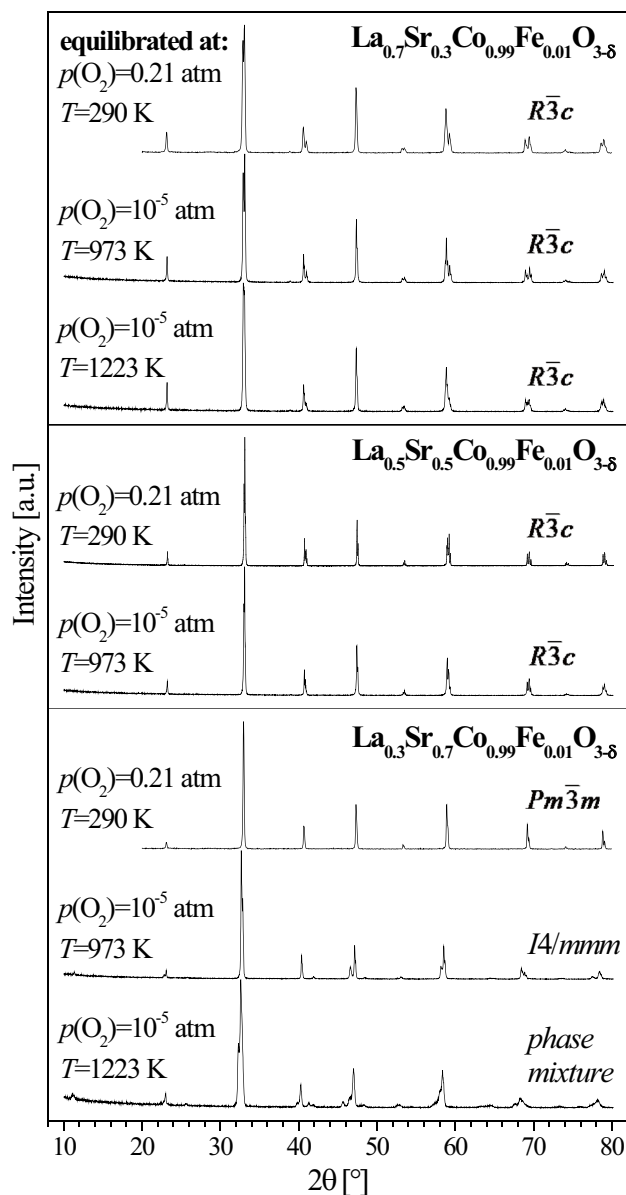


Fig. 4 X-ray diffraction patterns of powdered of $\text{La}_{1-x}\text{Sr}_x\text{Co}_{0.99}\text{Fe}_{0.01}\text{O}_{3-\delta}$ slowly cooled down to room temperature in air or quenched after annealing at 973–1223 K in flowing Ar, $p(\text{O}_2)\approx 10^{-5}$ atm

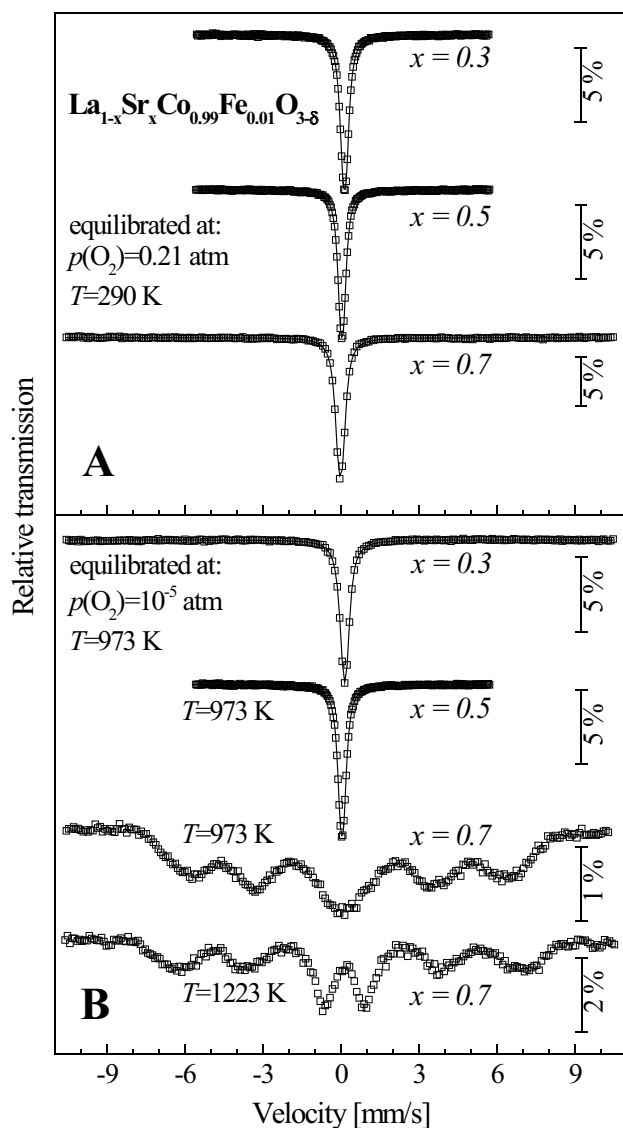


Fig. 5 Room-temperature Mössbauer spectra of $\text{La}_{1-x}\text{Sr}_x\text{Co}_{0.99}\text{Fe}_{0.01}\text{O}_{3-\delta}$ slowly cooled down to room temperature in air **A** and annealed at 973–1223 K in flowing Ar, $p(\text{O}_2) \approx 10^{-5}$ atm **B**. The solid lines show the fitting results (see text)

MossWinn software [26]. The room-temperature spectra were fitted to Lorentzian lines using a non-linear least-squares method; the relative areas and widths of both peaks in a quadrupole doublet were kept equal during refinement. Distributions of magnetic splittings were fitted to the magnetically split spectra collected at 4 K according to the histogram method. The relative oxygen content in air was determined by TGA on cooling from 1223 to 298 K with ramp rate of 2 K/min and dwells every 50 K at 923–1223 K. The total oxygen content ($3-\delta$) was calculated from the sample weight after reduction in 10% H_2 -90% N_2 gas mixture at 1223–1373 K (Fig. 2). The dilatometric data were obtained in the conditions of continuous heating in air (ramp rate 3 K/min). The total

electrical conductivity was measured in air by the 4-probe DC method. The data on oxygen permeability were obtained at 1023–1223 K and the feed-side oxygen pressure (p_2) fixed at 0.21 atm (air); the permeate-side oxygen pressure (p_1) varied from 0.008 to 0.2 atm. The equipment and procedures used for materials characterization, were also detailed in previous reports ([9, 14–16, 22–25] and references cited).

Results and discussion

Crystal structure and states of B-site cations

XRD analysis of A-site stoichiometric $\text{La}_{1-x}\text{Sr}_x\text{CoO}_{3-\delta}$ and $\text{La}_{1-x}\text{Sr}_x\text{Co}_{0.99}\text{Fe}_{0.01}\text{O}_{3-\delta}$ prepared in air showed the formation of single perovskite-type phases with rhombohedral ($x=0.3$ and 0.5) or cubic ($x=0.7$) structure, while the A-site deficient cobaltites contained small (< 2 wt%) amounts of CoO impurity phase (Figs. 3 and 4; Table 1). The Mössbauer spectra of all the $\text{La}_x\text{Sr}_{1-x}\text{Co}_{0.99}\text{Fe}_{0.01}\text{O}_{3-\delta}$ ($x=0.3, 0.5$ and 0.7) samples, except $\text{La}_{0.3}\text{Sr}_{0.7}\text{Co}_{0.99}\text{Fe}_{0.01}\text{O}_{3-\delta}$ annealed in argon, show a single absorption peak at room temperature (Fig. 5) and a six-line pattern at 4 K. In the case of samples equilibrated in air, a comparison of the isomer shifts and magnetic hyperfine fields (IS and B_{hf} ; Table 2) with the literature values for other (La,Sr) (Co,Fe) $\text{O}_{3-\delta}$ materials [27–31] shows that the average oxidation state of iron cations is intermediate between 3+ and 4+, increasing with Sr content. The electronic state of Fe and Co cations remains delocalized down to 4 K, although the materials are magnetically ordered at this temperature. Delocalized electronic states in perovskite-type ferrites down to 4 K

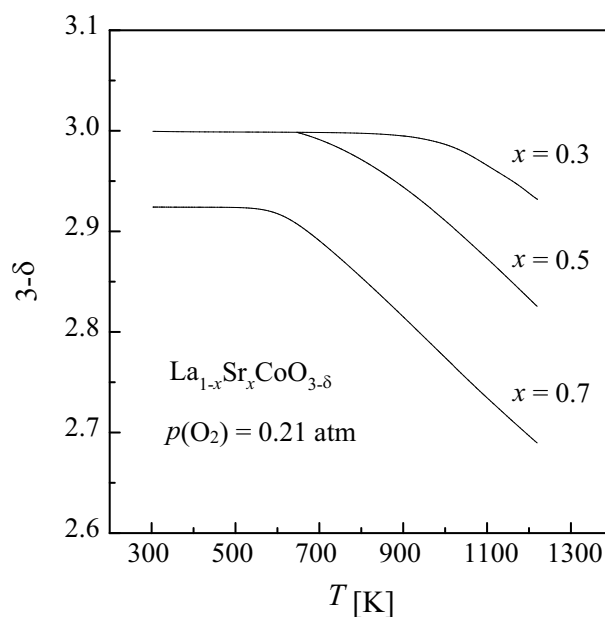


Fig. 6 Total oxygen content in $\text{La}_{1-x}\text{Sr}_x\text{CoO}_{3-\delta}$ measured by TGA in air using the reference point at 1223 K

Table 2 Parameters* estimated from the 4 K and 290 K Mössbauer spectra of $\text{La}_{1-x}\text{Sr}_x\text{Co}_{0.99}\text{Fe}_{0.01}\text{O}_{3-\delta}$ ceramics slowly cooled down to room temperature in air and annealed at 973–1223 K in flowing Ar

Composition	Equilibration conditions	T, K	Fe state	IS, mm/s	(QS/2ε), mm/s	B_{hf} , T	I, %
$\text{La}_{0.7}\text{Sr}_{0.3}\text{Co}_{0.99}\text{Fe}_{0.01}\text{O}_{3-\delta}$	$T=290\text{ K}$ $p(\text{O}_2)=0.21\text{ atm}$	4.1	$\text{Fe}^{3+/4+}$ CN = 6	0.34	−0.02	40.5	100
		290		0.25	0.13	-	100
$\text{La}_{0.5}\text{Sr}_{0.5}\text{Co}_{0.99}\text{Fe}_{0.01}\text{O}_{3-\delta}$		4.1	$\text{Fe}^{3+/4+}$ CN = 6	0.22	0.01	35.0	100
		290		0.15	0.12	-	100
$\text{La}_{0.3}\text{Sr}_{0.7}\text{Co}_{0.99}\text{Fe}_{0.01}\text{O}_{3-\delta}$		4.1	$\text{Fe}^{3+/4+}$ CN = 6	0.17	0.01	31.5	100
		290		0.09	0.16	-	100
$\text{La}_{0.7}\text{Sr}_{0.3}\text{Co}_{0.99}\text{Fe}_{0.01}\text{O}_{3-\delta}$	$T=973\text{ K}$ $p(\text{O}_2)\approx 10^{-5}\text{ atm}$	4.1	$\text{Fe}^{3+/4+}$ CN = 6	0.34	−0.02	40.5	100
		290		0.26	0.13	-	100
$\text{La}_{0.5}\text{Sr}_{0.5}\text{Co}_{0.99}\text{Fe}_{0.01}\text{O}_{3-\delta}$		4.1	$\text{Fe}^{3+/4+}$ CN = 6	0.22	−0.01	34.9	100
		290		0.15	0.12	-	100
$\text{La}_{0.3}\text{Sr}_{0.7}\text{Co}_{0.99}\text{Fe}_{0.01}\text{O}_{3-\delta}$	$T=1223\text{ K}$ $p(\text{O}_2)\approx 10^{-5}\text{ atm}$	4.1	Fe^{3+} CN = 6	0.45	0.19	50.6	57
			Fe^{3+} CN = 5	0.41	0.06	46.2	43
			Fe^{3+} CN = 6	0.45	0.26	51.8	36
			Fe^{3+} CN = 5	0.40	−0.05	46.6	36
			Fe^{3+} CN = 5,4	0.34	0.15	41.6	8
	$\text{Fe}^{2+/3+}$ CN = 5,4	0.53	−0.19	49.3	20		

* IS, B_{hf} , QS, ε, and I are the isomer shift relative to metallic α-Fe at 295 K, magnetic hyperfine field, quadrupole splitting, quadrupole shift, and relative area, respectively. For the 4.1 K spectra, the average IS and B_{hf} values are given. The estimated standard deviations are < 3% for I, < 0.2 T for B_{hf} , and < 0.02 mm/s for other parameters. CN is the oxygen-coordination number of Fe cations

have only been observed in the high-pressure (350–5000 atm) oxygen-annealed samples of cubic $\text{La}_{1-x}\text{Sr}_x\text{FeO}_3$ ($x=0.8\text{--}1.0$) with the oxygen content close to 3 [30, 31]. Usually in the perovskite-derived oxides containing Fe^{4+} , charge disproportionation $2\text{Fe}^{4+} \rightarrow \text{Fe}^{3+} + \text{Fe}^{5+}$ occurs on cooling and the electronic states become localized [24, 25, 30, 32]; the temperature of this disproportionation is higher than 4 K. However, in the Co-containing oxides with low content of anion vacancies when the concentration of cobalt is high enough, Fe^{4+} shows a delocalized electronic state down to 4 K, as in the oxidized $\text{La}_{0.33}\text{Sr}_{0.67}\text{Fe}_{0.4}\text{Co}_{0.6}\text{O}_3$ [33]. The combination of MS and TGA results (Fig. 6) suggests that in air up to 650 K, the incorporation of strontium in $\text{La}_x\text{Sr}_{1-x}\text{CoO}_{3-\delta}$ is essentially compensated by increasing oxidation state of B-site cations at $x \leq 0.5$, while the oxygen content is close to the stoichiometric, and by increasing both Co oxidation state and oxygen deficiency at higher temperatures and Sr concentrations.

The stability to reduction decreases on increasing Sr content (Fig. 4). Thus, $\text{La}_{0.3}\text{Sr}_{0.7}\text{Co}_{0.99}\text{Fe}_{0.01}\text{O}_{3-\delta}$ transforms from cubic to the tetragonal perovskite-type structure (space group $I4/mmm$) similar to that reported in Refs. [34, 35] after annealing in flowing Ar at $p(\text{O}_2)\approx 10^{-5}$ atm and 973 K and to the mixture of ordered tetragonal and disordered perovskite phases after annealing in the same atmosphere at 1223 K. $\text{La}_{0.7}\text{Sr}_{0.3}\text{Co}_{0.99}\text{Fe}_{0.01}\text{O}_{3-\delta}$ retains the rhombohedral perovskite structure in the entire range of these conditions. In accordance with the XRD data, the oxygen content variations in $\text{La}_{1-x}\text{Sr}_x\text{CoO}_{3-\delta}$ at elevated temperatures also

increase with x (Fig. 6). For $\text{La}_{0.7}\text{Sr}_{0.3}\text{Co}_{0.99}\text{Fe}_{0.01}\text{O}_{3-\delta}$ and $\text{La}_{0.5}\text{Sr}_{0.5}\text{Co}_{0.99}\text{Fe}_{0.01}\text{O}_{3-\delta}$, there is no difference between the Mössbauer spectra of the samples annealed in air and in argon atmosphere (Fig. 5) implying that partial reduction lowers primarily the oxidation state of cobalt cations. In the case of $\text{La}_{0.3}\text{Sr}_{0.7}\text{Co}_{0.99}\text{Fe}_{0.01}\text{O}_{3-\delta}$ annealed in Ar at 973 and 1223 K, resulting in the δ values close respectively to 0.37 and 0.48, broad absorption peaks are observed at 290 K indicating that the relaxation frequency of the direction of iron magnetic moments is of the same order of magnitude as the reciprocal of the Mössbauer time scale. This relaxation frequency may be explained by the establishment of long-range Fe–Fe or Fe–Co magnetic correlations above 290 K, while for all the other samples, these interactions were only established below room temperature. The Mössbauer spectra of reduced $\text{La}_{0.3}\text{Sr}_{0.7}\text{Co}_{0.99}\text{Fe}_{0.01}\text{O}_{3-\delta}$ with $\delta \approx 0.37$ at 4 K were fitted to two distributions of B_{hf} with different IS (Table 2) corresponding to hexa- and penta-coordinated Fe^{3+} [22, 23]. Note that the signal of remaining FeO_4 tetrahedra might overlap with the signal of pyramids. The 4 K spectrum of $\text{La}_{0.3}\text{Sr}_{0.7}\text{Co}_{0.99}\text{Fe}_{0.01}\text{O}_{3-\delta}$ with $\delta \approx 0.48$ consists of six broad absorption peaks and can only be analyzed with four sextets. Two main contributions with equal areas are related again to the tetragonal phase, while the remaining iron cations with the oxidation states equal to and lower than 3+ are in the disordered oxygen-deficient perovskite-related phase, in agreement with the XRD results. Even in the absence of phase transitions, presumable formation of point-defect clusters or vacancy-ordered microdomains

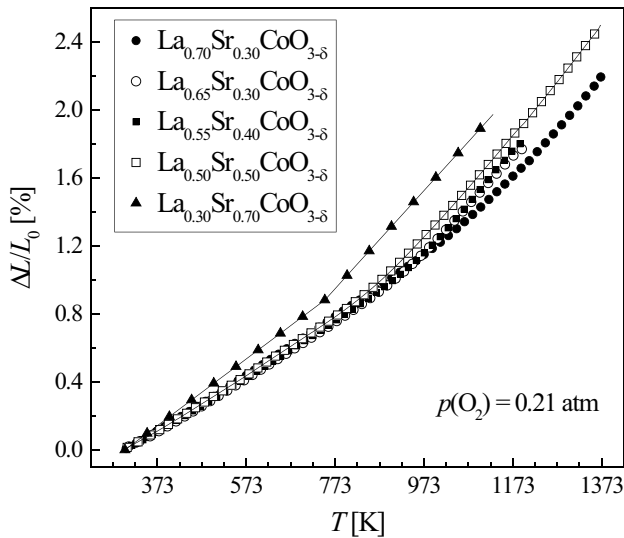


Fig. 7 Dilatometric curves of the sintered $\text{La}_{1-x}\text{Sr}_x\text{CoO}_{3-\delta}$ ceramics measured on continuous cooling in air

should have a significant influence on the thermomechanical and transport properties of cobaltite materials.

Lattice expansion and total electrical conductivity in air

Figure 7 presents the data on linear thermal expansion of $\text{La}_{1-x}\text{Sr}_x\text{CoO}_{3-\delta}$ ($x=0.3, 0.5$ and 0.7) and A-site-deficient $\text{La}_{0.95-x}\text{Sr}_x\text{CoO}_{3-\delta}$ ($x=0.3$ and 0.4) dense ceramics in air. These results are given relative to the sample length at room temperature (L_0). The average thermal expansion

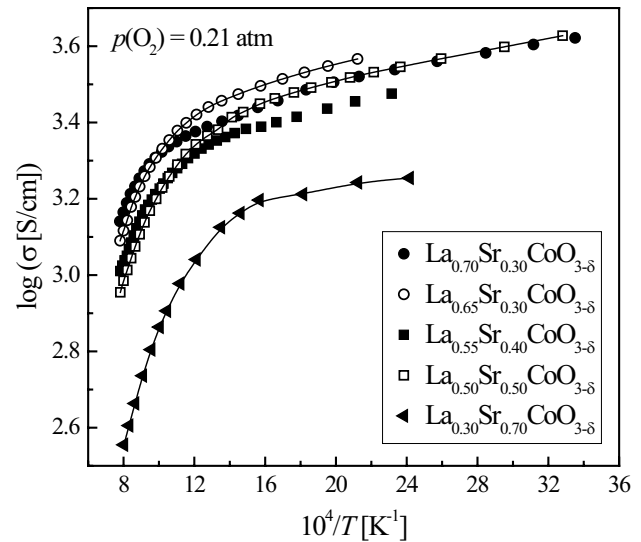


Fig. 8 Temperature dependencies of the total electrical conductivity of sintered $\text{La}_{1-x}\text{Sr}_x\text{CoO}_{3-\delta}$ ceramics in air

coefficients (TECs) are listed in Table 1. As for the other perovskite-type cobaltites [9, 36, 37], the dilatometric curves are characterized by a break at 750–1070 K with the drastic increase in the TEC values from $(16\text{--}17) \times 10^{-6} \text{ K}^{-1}$ up to $(28\text{--}31) \times 10^{-6} \text{ K}^{-1}$. This phenomenon originates from chemically induced expansion of the crystal lattice due to an increase in the oxygen nonstoichiometry. Correspondingly, the oxidation states of B-site cations decrease and their size increases. In addition, increasing the oxygen deficiency leads to a higher coulombic repulsion between positively charged oxygen vacancies and holes, and also to an increase

Table 3 Summary of selected regression models for $p(\text{O}_2)$ - T - δ diagrams of $\text{La}_{1-x}\text{Sr}_x\text{CoO}_{3-\delta}$

Model	Brief description	General formulation	Specific parameters
Model 1	Rigid-band based on hole chemical potential; electron-vacancy association	$\mu(\text{h}) = \mu(\text{h}^0) + \frac{[\text{h}^-] - [\text{h}^0]}{g(\mu(\text{h}^0))}$, $[\text{h}^0] = [\text{Sr}'_A]$,	$N(\delta) = [O_o^\Sigma] = 3$
Model 2	Rigid-band based on hole chemical potential, with site-exclusions; electron-vacancy association	$\mu'(V_o^\bullet) = RT \ln \frac{[V_o^\bullet]}{N(\delta) - \delta}$, $\mu'(\langle V_o - \text{Co}_B \rangle) = RT \ln \frac{[V_o - \text{Co}_B]}{N(\delta) - \delta}$	$N(\delta) = [O_o^\Sigma] \left(1 - \frac{\delta}{O_o^\Sigma}\right)^n$ $n = 8, 10, > 10$
Model 3	Model 1 but based on $\langle V - \text{Co} \rangle$ chemical potential, no V_o^\bullet near Co'	$\mu'(\langle V_o - \text{Co}_B \rangle) = RT \ln \frac{[V_o - \text{Co}_B]}{N(\langle V_o - \text{Co}_B \rangle) - (\langle V_o - \text{Co}_B \rangle)}$	$N(\langle V_o - \text{Co}_B \rangle) = \left(1 - \frac{\delta}{3}\right)^n$ $n = 5$
Model 4	Rigid-band based on hole chemical potential; Co self-ionization at $\delta \rightarrow 0$	$\mu(\text{h}') = \mu(\text{h}^0) + \frac{[\text{h}^-] - [\text{h}^0]}{g(\mu(\text{h}^0))}$, \dots $[\text{h}^0] = [\text{Sr}'_A]$,	$N(\delta) = [O_o^\Sigma] = 3$
Model 5	Model 4 with site-exclusions	$\mu'(V_o^\bullet) = RT \ln \frac{[V_o^\bullet]}{N(\delta) - \delta}$, $K_{pm} = a(\text{h}')a(\text{Co}_B)$	$N(\delta) = [O_o^\Sigma] \left(1 - \frac{\delta}{O_o^\Sigma}\right)^n$

* Kröger-Vink notation is used and all concentration-related terms are normalized to one formula unit

** μ is the chemical potential consisting of concentration-dependent (μ') and concentration-independent (μ^0) parts, $[\text{h}^0]$ is the electron-hole concentration at zero δ , $g(\mu(\text{h}^0))$ is the electronic density of states at the Fermi level, $[V_o^\bullet]$ is the concentration of mobile oxygen vacancies, δ is the total concentration of vacant oxygen sites measured by TGA and coulometric titration [14], $N(\delta)$ is the corresponding number of states, and n is the number of sites in vacancy neighborhood excluded from ionic transport; for perovskites the minimal value for n is 8 (nearest neighbors), the next value is 10 (2 additional sites from shared octahedra) and further depending on infill of coordination spheres

in the anharmonicity of atomic vibrations [38]. All these effects expand the crystal lattice. In agreement with the oxygen content variations (Fig. 6), decreasing La content shifts this break to lower temperatures and results in higher TECs.

The lattice expansion of $\text{La}_{1-x}\text{Sr}_x\text{CoO}_{3-\delta}$ correlates with the data on total electrical conductivity (Fig. 8), predominantly p-type electronic in air. A progressive increase in the oxygen deficiency leads, in particular, to a lower concentration of electron holes and thus decreases the conductivity when temperature increases. Below ~ 980 K $\text{La}_{0.65}\text{Sr}_{0.30}\text{CoO}_{3-\delta}$ exhibits the maximum conductivity. In the higher-temperature range, the σ values increase on lanthanum content. Nevertheless, the level of electronic conduction is nearly similar for all compositions with $x < 0.7$, being significantly higher than that in $\text{La}_{0.3}\text{Sr}_{0.7}\text{CoO}_{3-\delta}$ (Fig. 8) in the entire temperature range. In the latter, the charge compensation mechanism via the oxygen vacancy formation on Sr^{2+} doping starts to prevail. Another effect may be associated with the ordering processes in the oxygen sublattice. Note that the formation of vacancy-ordered microdomains would be undetectable by XRD. These processes are, however, visible from the oxygen permeability results discussed below.

Modeling $p(\text{O}_2)$ - T - δ diagrams

The experimental data on the oxygen nonstoichiometry variations in $\text{La}_{1-x}\text{Sr}_x\text{CoO}_{3-\delta}$ ($x = 0.3$ – 0.7) vs. oxygen partial pressure and temperature, determined by coulometric titration, are taken from Tsipis et al. [14]. These data were modeled taking into account significant influence of the vacancy association phenomena on the oxygen thermodynamics of $(\text{La},\text{Sr})\text{CoO}_{3-\delta}$, which becomes critical on reduction. The models presupposing pair clusters are simplest from the statistical point of view and thus provide minimum errors in the entire $p(\text{O}_2)$ range. A brief formulation of selected statistical-thermodynamic models used to analyze the equilibrium $p(\text{O}_2)$ - T - δ diagrams is summarized in Table 3. All these models included the contribution of delocalized electron holes, described in the framework of rigid-band approach. If the generation of p-type charge carriers is significantly affected by intrinsic electronic disordering when Co'_B exists predominantly in the form of any clusters with oxygen vacancies, such as $\langle V_O - \text{Co}_B \rangle$, the electron-hole concentration at zero δ , $[h^0]$, is equal to Sr'_A (hereafter see definitions after Table 3). The expressions for the concentration-dependent parts of the chemical potentials of vacancies and $\langle V_O - \text{Co}_B \rangle$ clusters are the same for Models 1 and 2. In the simplest case when all oxygen sites are energetically equivalent and vacancy interaction can be neglected (Model 1), the number of states for oxygen vacancies $N(\delta)$ is equal to the number of oxygen sites. When the site-exclusion effects caused by coulombic repulsion between the vacancies are significant (Model 2), $N(\delta)$ is determined by the probability of complete occupation of n neighboring oxygen sites. If no vacancy can

be located in the first coordination sphere near a vacant site, $n = 8$. For Models 1 and 2, the Co'_B species were considered as polarons localized near oxygen vacancies, forming stable pair clusters $\langle V_O - \text{Co}_B \rangle$. In this case, the site-conservation and electroneutrality conditions can be expressed as

$$\delta + [\text{O}_o^\times] = [\text{O}_o^\ominus] = 3 \text{ and } [\langle V_O - \text{Co}_B \rangle] + [\text{V}_o^{\cdot\cdot}] = \delta \quad (1)$$

$$[h^\cdot] + [\langle V_O - \text{Co}_B \rangle] + 2[\text{V}_o^{\cdot\cdot}] = \text{Sr}'_A \quad (2)$$

whilst the electron-hole recombination processes should correlate with the oxygen nonstoichiometry:

$$\text{Co}_B^\times + \text{V}_o^{\cdot\cdot} \rightleftharpoons h^\cdot + \langle V_O - \text{Co}_B \rangle \quad K_1 = \frac{a(\text{V}_o^{\cdot\cdot})}{a(h^\cdot)a(\langle V_O - \text{Co}_B \rangle)} \quad (3)$$

where a is the thermodynamic activity and K is the equilibrium constant. Hereafter, the concentration of regular Co_B^\times sites is considered constant. One modification of this formalism, referred to as Model 3, was similar to Model 1 but

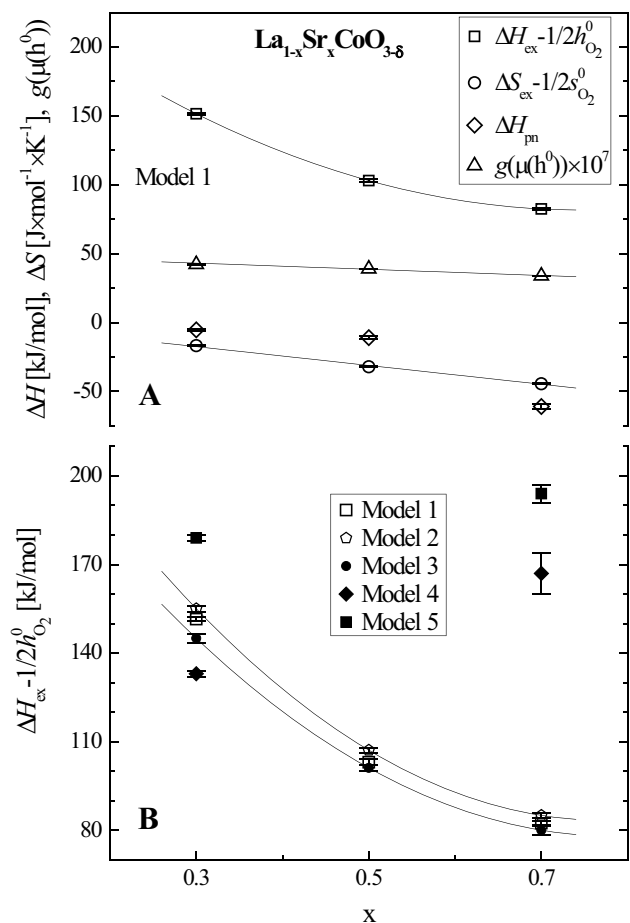
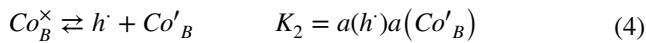
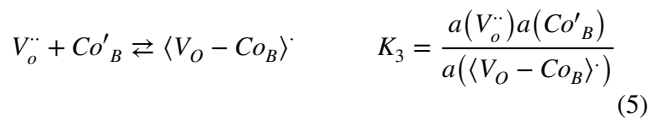


Fig. 9 Parameters of the regression models for $p(\text{O}_2)$ - T - δ diagrams of $\text{La}_{1-x}\text{Sr}_x\text{CoO}_{3-\delta}$; 422, 420, and 348 points were included in the analysis for $x = 0.3$, 0.5 , and 0.7 , respectively

presumed that clustering is governed by the cobalt sublattice (Table 3). Here $n = 5$ implies that no other vacancies may form near $\langle V_O - Co_B \rangle$ cluster. Finally, Models 4 and 5 were based on Models 1 and 2, respectively, disregarding formation of the $\langle V_O - Co_B \rangle$ clusters but accounting for cobalt disproportionation. This reaction shifts $[h^0]$ and leads to the existence of free Co'_B :



with the concentration-dependent part of chemical potential expressed as $RT \ln([Co'_B]/[Co_B^{\times}])$. In this case, the $\langle V_O - Co_B \rangle$ formation might be considered as an additional process:



However, extension of the Models 4 and 5 with Eq. (5) leads to degeneration of the least squares statistics; the results for these extended models were hence omitted.

Parameters obtained from the regression analysis by Models 1–5 are compared in Fig. 9 and Table 4; the residuals scatter is illustrated in Fig. S1 (Electronic Supplementary Material). Model 1 was found to provide the best description of the experimental data. Figure 10 presents the oxygen pressure dependencies of the defect concentrations calculated using this model. As expected, partial reduction lowers the concentration of electron holes and increases the concentration of $\langle V_O - Co_B \rangle$ clusters, whereas the number of free oxygen vacancies, $[V_o^{\cdot\cdot}]$, remains low with a tendency to pass through a maximum or even decrease. The calculated concentrations of mobile oxygen vacancies were used to analyze the oxygen permeability of dense $La_{1-x}Sr_xCoO_{3-\delta}$ ceramic membranes.

Table 4 Parameters* obtained from the analysis of $p(O_2)$ - T - δ diagrams of $La_{1-x}Sr_xCoO_{3-\delta}$

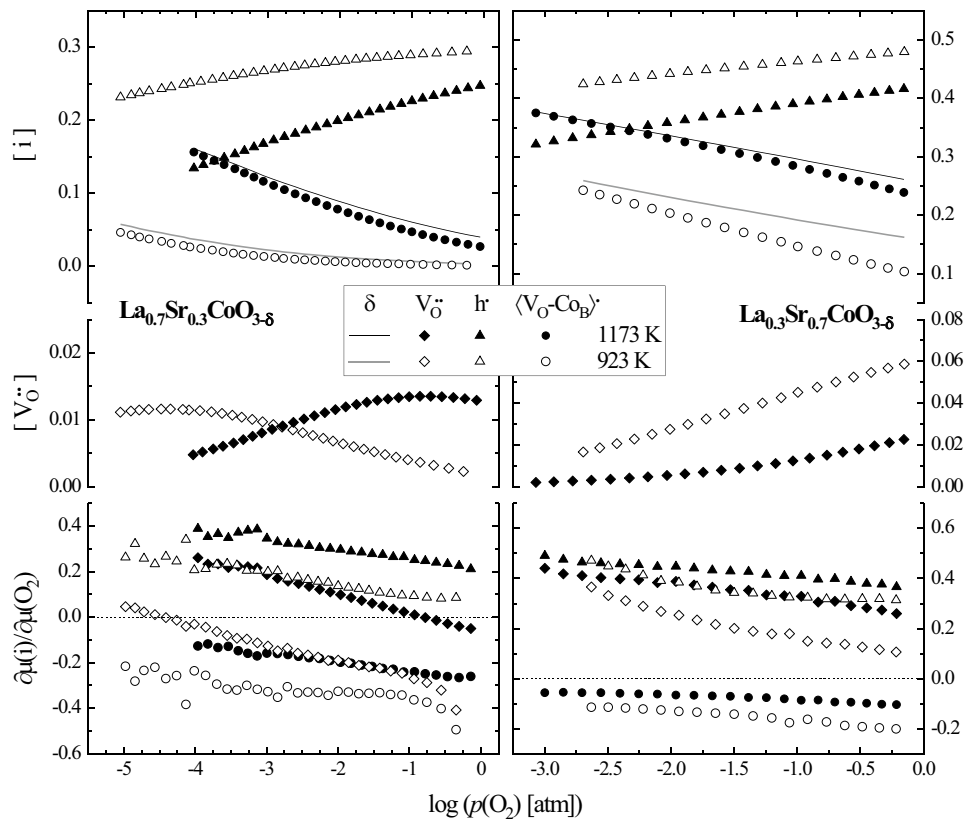
x	$(\Delta H_{ex} - \frac{1}{2}h_{O_2}^0)$ kJ \times mol $^{-1}$	$(\Delta S_{ex} - \frac{1}{2}s_{O_2}^0)$ J \times mol $^{-1}$ \times K $^{-1}$	ΔH_i kJ \times mol $^{-1}$	$g(\mu(h^0)) \times 10^7$ kJ $^{-1}$ \times mol	$\Delta\delta \times 10^3$	R_{adj}	N_{points}
Model 1							
0.3	151.5 \pm 0.7	-16.8 \pm 0.6	-5.3 \pm 0.5**	42.2 \pm 0.5	20.8 \pm 0.2 ($T > 898$ K) 19.8 \pm 0.1 ($T = 898$ K) 18.7 \pm 0.1 ($T = 873$ K)	0.9995	422
0.5	103 \pm 1	-32.2 \pm 0.5	-11 \pm 1**	38.9 \pm 0.2	-	0.9996	420
0.7	82.4 \pm 0.6	-44.5 \pm 0.4	-61 \pm 2**	33.8 \pm 0.3	-	0.9996	348
Model 2							
0.3	155 \pm 1	-16.9 \pm 0.7	-6.9 \pm 0.6**	52 \pm 1	20.7 \pm 0.1 ($T > 898$ K) 19.6 \pm 0.1 ($T = 898$ K) 18.6 \pm 0.1 ($T = 873$ K)	0.9995	422
0.5	107.1 \pm 0.9	-29.0 \pm 0.6	-11.9 \pm 0.8**	44.1 \pm 0.8	-	0.9994	420
0.7	85 \pm 1	-37.1 \pm 0.4	-48 \pm 3**	42 \pm 1	-	0.9996	348
Model 3							
0.3	145 \pm 2	-12 \pm 1	0 \pm 1**	57 \pm 3	20.2 \pm 0.2 ($T > 873$ K) 18.7 \pm 0.2 ($T = 873$ K)	0.9990	422
0.5	101 \pm 1	-19.3 \pm 0.7	-5.0 \pm 0.8**	44.8 \pm 0.3	-	0.9993	420
0.7	80 \pm 2	-30.3 \pm 0.6	-37 \pm 3**	49 \pm 1	-	0.9993	348
Model 4							
0.3	133 \pm 1	-24 \pm 1	-35.5 \pm 0.8***	79 \pm 5	20.1 \pm 0.3 ($T > 898$ K) 19.4 \pm 0.2 ($T = 898$ K) 18.7 \pm 0.2 ($T = 873$ K)	0.9990	422
0.7	167 \pm 7	-67 \pm 3	-69 \pm 2***	196 \pm 7	-	0.970	348
Model 5							
0.3	179 \pm 1	-24.7 \pm 0.5	-25.8 \pm 0.5***	0.4 \pm 4	21.6 \pm 0.3 ($T > 898$ K) 20.6 \pm 0.3 ($T = 898$ K) 19.4 \pm 0.3 ($T = 873$ K)	0.9993	422
0.7	194 \pm 3	-47 \pm 2	-78 \pm 1***	148 \pm 4	-	0.990	348

* ΔH_{ex} and ΔS_{ex} are the enthalpy and entropy of oxygen deintercalation, $h_{O_2}^0$ and $s_{O_2}^0$ are the enthalpy and entropy of gaseous molecular oxygen (IUPAC), $g(\mu(h^0))$ is the electronic density of states at the Fermi level, and $\Delta\delta$ is the parameter that may comprise systematic errors of TGA. Errors are for 95% confidence. R_{adj} is the adjusted correlation coefficient, and N_{points} is the number of experimental points included in the analysis

** $\Delta H_i = \Delta H_1$ is the enthalpy of electron-hole recombination process near oxygen vacancy according to Eq. (3)

*** $\Delta H_i = \Delta H_2$ is the enthalpy of Co_B^{\times} disproportionation according to Eq. (4)

Fig. 10 Oxygen partial pressure dependencies of the defect concentrations and derivatives of the defect chemical potential with respect to the oxygen chemical potential at 923 and 1173 K, calculated using Model 1 (see Table 3) for the analysis of $p(\text{O}_2)$ - T - δ diagrams of $\text{La}_{1-x}\text{Sr}_x\text{CoO}_{3-\delta}$ ($x=0.3$ and 0.7)



Surface-limited oxygen permeability and ionic conductivity

The steady-state oxygen permeation fluxes (j) through the dense $\text{La}_{1-x-y}\text{Sr}_x\text{CoO}_{3-\delta}$ ceramics generally increase with increasing strontium content and oxygen deficiency (Fig. 11), while the corresponding activation energies decrease (Table 1). The role of surface oxygen exchange kinetics evaluated from the oxygen flux dependencies on membrane thickness (d) also increases with x and becomes critical at $x \geq 0.5$. For instance, at $x = 0.3$, the products $j \times d$ are essentially thickness-independent (Fig. 12), indicating that the oxygen permeation is limited by the bulk ionic transport. At $x = 0.5$ both permeation fluxes and $j \times d$ depend on the membrane thickness. The permeation fluxes through 1.0- and 1.4 mm-thick $\text{La}_{0.3}\text{Sr}_{0.7}\text{CoO}_{3-\delta}$ membranes are similar, suggesting the dominant role of surface exchange limitations [14]. Therefore, the oxygen transport processes were modeled by splitting the overall oxygen chemical potential gradient into three parts corresponding to the membrane bulk ($\Delta\mu^{\text{bulk}}$), permeate-side ($\Delta\mu_1^{\text{surf}}$), and feed-side ($\Delta\mu_2^{\text{surf}}$), as illustrated in Figs. 13 and 14. The basic formulations of selected models used for nonlinear regression analysis are summarized in Table 5. The bulk contribution determined by the partial ionic (σ_{O}) and electronic (σ_e) conductivities was calculated by solving the Wagner equation. Since the electronic conductivity

in lanthanum-strontium cobaltites is prevailing over ionic, the ambipolar conductivity may be equated to σ_{O} . For the materials with $x \geq 0.5$ when the oxygen fluxes

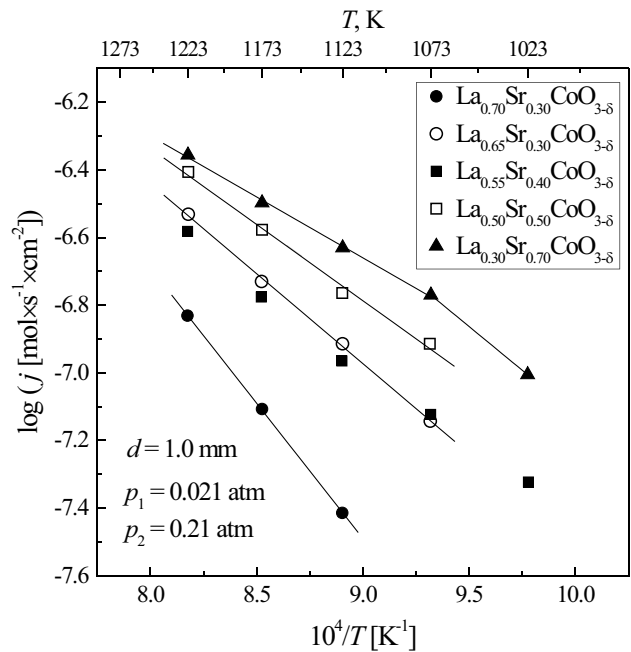


Fig. 11 Temperature dependencies of the oxygen permeation fluxes through 1.0 mm-thick $\text{La}_{1-x-y}\text{Sr}_x\text{CoO}_{3-\delta}$ membranes at fixed oxygen partial pressure gradient. Solid lines are for visual guidance

are surface-limited, the oxygen transfer across the membrane/gas interfaces was simulated using phenomenological expressions given in Table 5. These expressions were selected on the basis of fitting results from a number of alternative approaches, including the Butler-Volmer type models and various kinetic and thermodynamic equations [39, 40], and represent simplified solutions of the general thermodynamic formulae, where the transport coefficient \mathfrak{R}_i may comprise concentration of species involved in the rate-determining steps. The driving force in these equations (Table 5) is expressed as $\Delta\mu_i^{surf}/z$. The best fitting quality was obtained fixing $z=2$, which implies the limiting role of oxygen vacancies and/or adsorbed atomic species in the total oxygen transport through membrane boundaries, in agreement with van Doorn et al. [6].

In the course of regression analysis of the oxygen permeation data of $\text{La}_{1-x}\text{Sr}_x\text{CoO}_{3-\delta}$ ($x=0.3-0.7$), the set of equations was solved numerically using the relationships between $[V_o^{\bullet\bullet}]$, $[O_o^{\times}]$, and $\mu(\text{O}_2)$ defined from the analysis of $p(\text{O}_2)$ - T - δ diagrams (Table 4). For $\text{La}_{0.7}\text{Sr}_{0.3}\text{CoO}_{3-\delta}$, where under the studied conditions the oxygen permeation

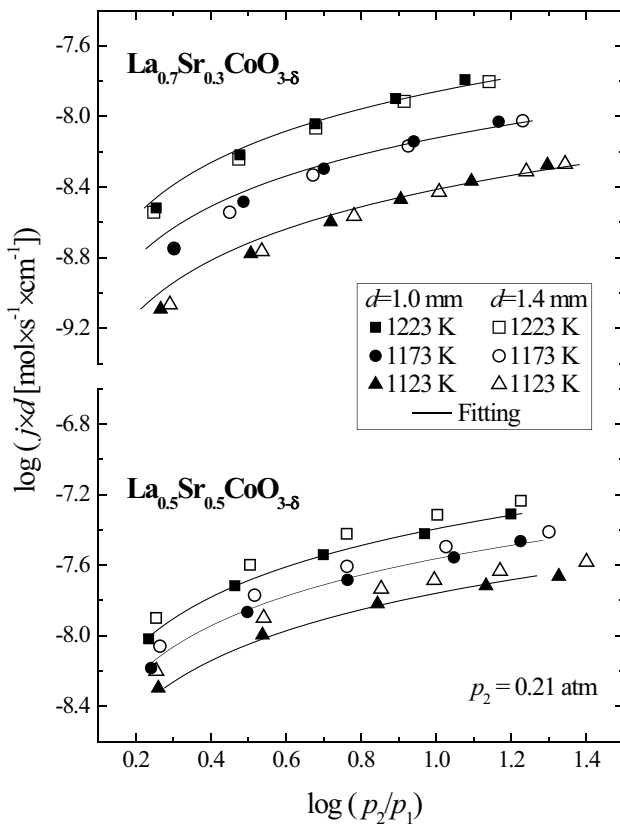


Fig. 12 Products of steady-state oxygen permeation fluxes through dense $\text{La}_{1-x}\text{Sr}_x\text{CoO}_{3-\delta}$ ($x=0.3$ and 0.5) membranes and membrane thickness (d) as a function of the oxygen partial pressure gradient. $d=1.00\pm 0.02$ and 1.40 ± 0.02 mm. Solid lines show the fitting results (see text)

is limited by the bulk ionic transport, $\Delta\mu_1^{surf} = \Delta\mu_2^{surf} = 0$. The regression parameters calculated using selected models are compared in Figs. 15 and 16 and Table 6. The results of fitting to the best models shown in Fig. 12 as solid lines are in a reasonable agreement with the experimental data. For the bulk ionic transport, all considered models provided comparable and satisfactory fitting quality. The simplest model neglecting the long-range ordering phenomena and coulombic repulsion is suggested as most appropriate (hereafter see definitions in the bottom caption of Table 5):

$$\sigma_o = U_o [V_o^{\bullet\bullet}] [O_o^{\times}] \quad (6)$$

Further complications did not result in any essential improvement of the fitting quality. In the case of $\text{La}_{0.3}\text{Sr}_{0.7}\text{CoO}_{3-\delta}$, the models for oxygen fluxes across the membrane feed and permeate sides, expressed respectively as

$$j = J_2^0 \delta \left(1 - \exp\left(\frac{\Delta\mu_2^{surf}}{2RT}\right) \right) \quad (7)$$

$$j = J_1^0 \frac{\Delta\mu_1^{surf}}{2RT} \quad (8)$$

gave the best fitting results. For $\text{La}_{0.5}\text{Sr}_{0.5}\text{CoO}_{3-\delta}$ the only approach enabling to fit the data at all studied temperatures was based on the assumption that the surface oxygen exchange limitations occur exclusively at the membrane

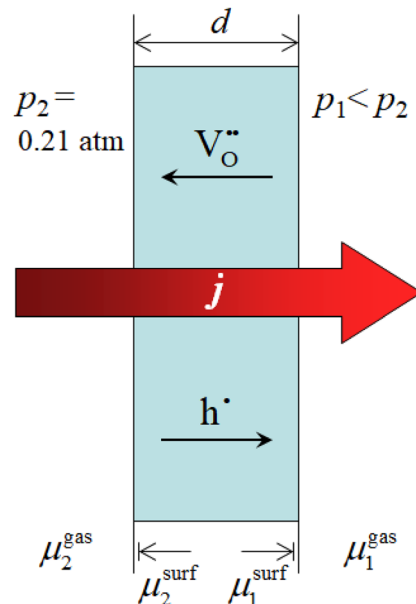


Fig. 13 Schematic drawing illustrating the fluxes of charge carriers through the mixed-conducting membrane and the oxygen chemical potentials at the membrane surfaces and in the gas phase

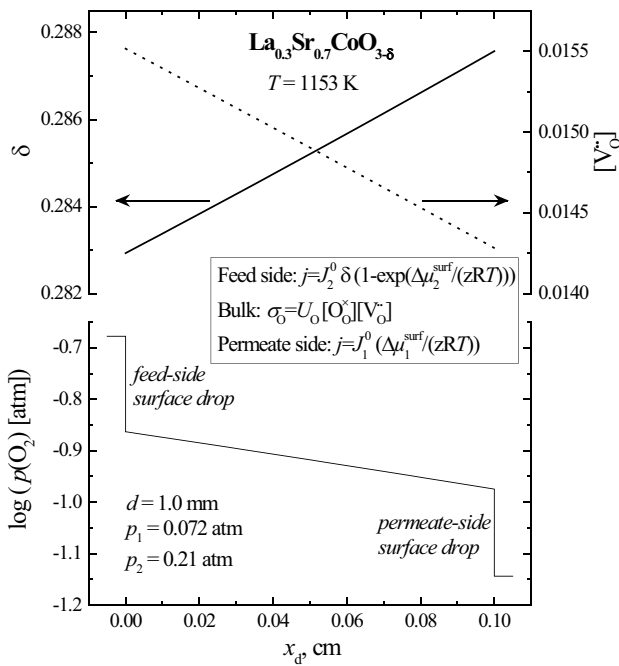


Fig. 14 Variations of oxygen nonstoichiometry and concentration of mobile oxygen vacancies across the thickness of $\text{La}_{0.3}\text{Sr}_{0.7}\text{CoO}_{3-\delta}$ membrane under the oxygen pressure gradient of 0.072/0.21 atm at 1153 K, and the corresponding oxygen pressure profile calculated using the models S1, B1, and S3 with $z=2$ for the membrane feed side, bulk and permeate side, respectively (see Table 5)

permeate side, as expressed by Eq. (8). At this side, the oxygen chemical potential gradient is found lower compared to that across the bulk (Fig. 17). The difference, however, decreases on cooling as a result of increasing role of oxygen exchange kinetics.

Figure 18 compares the oxygen partial pressure dependencies of calculated ionic conductivity of $\text{La}_{1-x}\text{Sr}_x\text{CoO}_{3-\delta}$

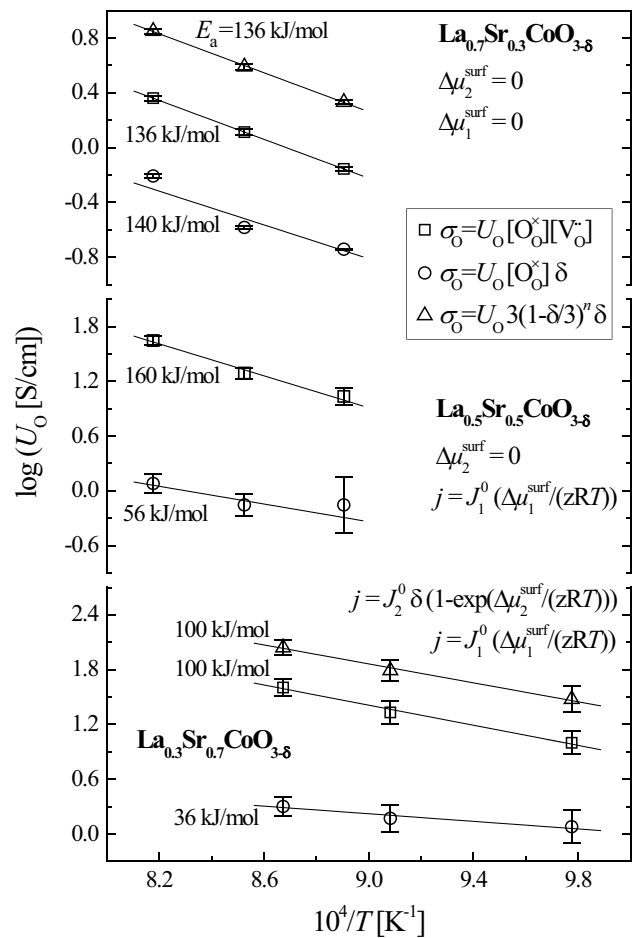


Fig. 15 Temperature dependence of the constant involving oxygen ion mobility calculated from the modeling results of oxygen permeability data of $\text{La}_{1-x}\text{Sr}_x\text{CoO}_{3-\delta}$ at $z=2, n=10$ (see Tables 5 and 6)

($x=0.3$ and 0.7) at 1023 and 1173 K. For $\text{La}_{0.7}\text{Sr}_{0.3}\text{CoO}_{3-\delta}$ where the δ values are moderate, decreasing $p(\text{O}_2)$ results in the formation of both free oxygen vacancies and

Table 5 Summary of selected regression models for oxygen permeability of the $\text{La}_{1-x}\text{Sr}_x\text{CoO}_{3-\delta}$ dense ceramic membranes

Location	General formulation	Specific parameters	Model
Bulk	$j = \frac{1}{16F^2d} \int \frac{\mu_2^{surf}}{\sigma_o + \sigma_e} d\mu(\text{O}_2)$	$N_o = [\text{O}_o^\times], N_v = [\text{V}_o^\cdot]$	B1
	$\lim_{\sigma_e \gg \sigma_o} \frac{\sigma_o \sigma_e}{\sigma_o + \sigma_e} = \sigma_o, \sigma_o = U_o N_o N_v$	$N_o = [\text{O}_o^\times], N_v = \delta$	B2
		$N_o = 3 \left(1 - \frac{N_v}{3}\right)^n, N_v = \delta, n = 10$	B3
Boundary	$J = \mathfrak{R} \left(1 - \exp\left(\frac{\Delta\mu^{surf}}{zRT}\right)\right), \mathfrak{R} = J^0 f(c_{lim})$	$f(c_{lim}) = \delta, z = 2$	S1
		$f(c_{lim}) = 1, z = 2$	S2
	$J = \mathfrak{R} \frac{\Delta\mu^{surf}}{zRT}, \mathfrak{R} = J^0 f(c_{lim})$	$f(c_{lim}) = 1, z = 2$	S3

* U_o is the temperature-dependent constant involving oxygen ion mobility, N_o is the number of neighboring occupied oxygen sites appropriate for a swap with unoccupied sites, N_v is the number of unoccupied oxygen sites available for ion jumping, $\Delta\mu^{surf}$ is the drop of oxygen chemical potential across considered border, \mathfrak{R} , is the limiting flux density, $f(c_{lim})$ is the concentration-dependent configurational term in \mathfrak{R} , J_o is the temperature-dependent constant and z is the stoichiometric coefficient showing relationships between the fluxes of molecular O_2 and species involved in the rate-determining step

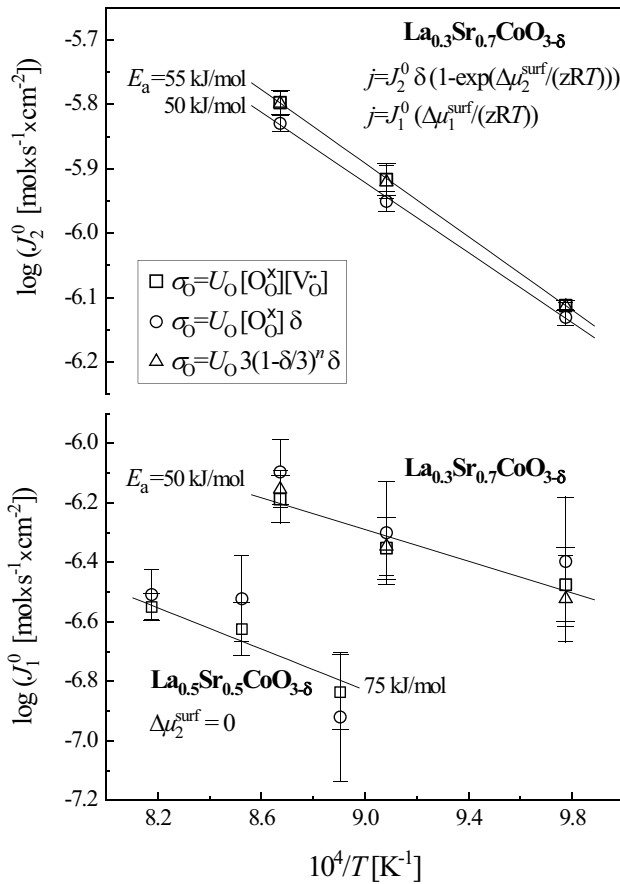


Fig. 16 Comparison of temperature dependencies of the parameters of regression models for oxygen permeability of the $\text{La}_{1-x}\text{Sr}_x\text{CoO}_{3-\delta}$ ($x=0.5$ and 0.7) membranes at the feed- and permeate-side surfaces using three different models for the bulk ionic transport; $z=2$, $n=10$ (see Tables 5 and 6)

$\langle V_O - Co_B \rangle$ clusters (Eq. (3)). Consequently, on reduction the ionic conductivity first increases, then passes through a maximum and decreases when the generation of defect associates becomes prevailing, in agreement with the $[V_o^{\bullet}]$ variations (Fig. 10). These maxima shift to lower oxygen pressures on cooling in agreement with the literature data on $\text{La}_{0.4}\text{Sr}_{0.6}\text{CoO}_{3-\delta}$ [11, 12]. At higher x and δ values in $\text{La}_{1-x}\text{Sr}_x\text{CoO}_{3-\delta}$, the tendency of defect association becomes more pronounced (Fig. 10). A break at 1073 K in the Arrhenius plot of the oxygen permeation fluxes through the $\text{La}_{0.3}\text{Sr}_{0.7}\text{CoO}_{3-\delta}$ ceramics (Fig. 11) indicates the oxygen-vacancy ordering processes [9] becoming finally long-range at lower oxygen partial pressures as revealed by

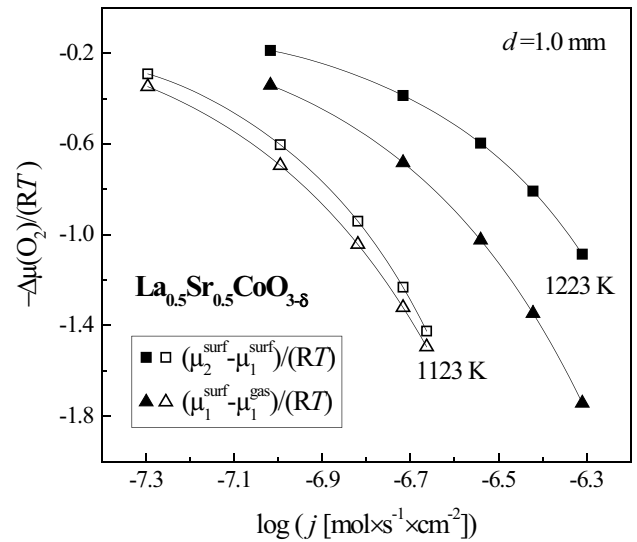


Fig. 17 Oxygen chemical potential gradients across the bulk and permeate-side surface of 1.0 mm-thick $\text{La}_{0.5}\text{Sr}_{0.5}\text{CoO}_{3-\delta}$ membrane at 1123 and 1223 K plotted against the steady-state oxygen permeation fluxes

the XRD and MS analyses. Correspondingly, the oxygen ionic conductivity monotonically decreases on reduction in the experimentally studied $p(\text{O}_2)$ range (Fig. 18).

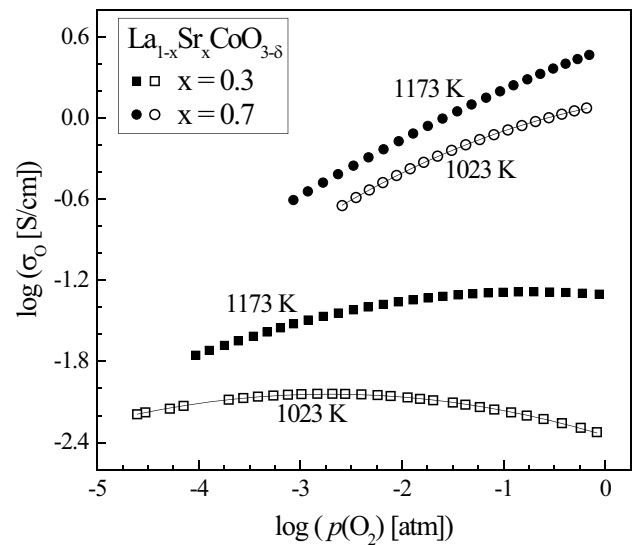


Fig. 18 Oxygen partial pressure dependencies of the ionic conductivity in $\text{La}_{0.7}\text{Sr}_{0.3}\text{CoO}_{3-\delta}$ and $\text{La}_{0.3}\text{Sr}_{0.7}\text{CoO}_{3-\delta}$ calculated from the fitting results of the oxygen nonstoichiometry and permeability data at 1023 and 1173 K

Table 6 Parameters of the selected regression models for oxygen permeability of $\text{La}_{1-x}\text{Sr}_x\text{CoO}_{3-6}$ dense ceramic membranes

Model	Parameter	T, K	E_a , kJ/mol
$\text{La}_{0.7}\text{Sr}_{0.3}\text{CoO}_{3-6}$		1223	1123
Both feed and permeate sides are under equilibrium			
Bulk: Model B1	$U_O, S \times \text{cm}^{-1}$	2.30 ± 0.09	1.30 ± 0.06
	R_{adj}	0.990	0.98
Bulk: Model B2	$U_O, S \times \text{cm}^{-1}$	0.62 ± 0.02	0.181 ± 0.002
	R_{adj}	0.997	0.9994
Bulk: Model B3	$U_O, S \times \text{cm}^{-1}$	7.1 ± 0.3	2.15 ± 0.08
	R_{adj}	0.990	0.990
		1223	1123
$\text{La}_{0.5}\text{Sr}_{0.5}\text{CoO}_{3-6}$			
Feed: equilibrium	-		
Bulk: Model B1	$U_O, S \times \text{cm}^{-1}$	44 ± 5	11 ± 2
Permeate: Model S3	$J_1^0, \mu\text{mol} \times \text{s}^{-1} \times \text{cm}^{-2}$	0.28 ± 0.03	0.15 ± 0.04
	R_{adj}	0.9990	0.994
Feed: Model S1	$J_2^0, \mu\text{mol} \times \text{s}^{-1} \times \text{cm}^{-2}$		2.2 ± 0.2
Bulk: Model B1	$U_O, S \times \text{cm}^{-1}$		11.7 ± 0.8
Permeate: Model S3	$J_1^0, \mu\text{mol} \times \text{s}^{-1} \times \text{cm}^{-2}$		0.26 ± 0.05
	R_{adj}		0.9992
Feed: equilibrium	-		
Bulk: Model B2	$U_O, S \times \text{cm}^{-1}$	1.2 ± 0.3	0.7 ± 0.5
Permeate: Model S3	$J_1^0, \mu\text{mol} \times \text{s}^{-1} \times \text{cm}^{-2}$	0.31 ± 0.06	0.12 ± 0.06
	R_{adj}	0.998	0.990
		1153	1023
$\text{La}_{0.3}\text{Sr}_{0.7}\text{CoO}_{3-6}$			
Feed: Model S1	$J_2^0, \mu\text{mol} \times \text{s}^{-1} \times \text{cm}^{-2}$	1.59 ± 0.07	0.77 ± 0.01
Bulk: Model B1	$U_O, S \times \text{cm}^{-1}$	40 ± 9	10 ± 3
Permeate: Model S3	$J_1^0, \mu\text{mol} \times \text{s}^{-1} \times \text{cm}^{-2}$	0.6 ± 0.1	0.3 ± 0.1
	R_{adj}	0.9991	0.9994
Feed: Model S1	$J_2^0, \mu\text{mol} \times \text{s}^{-1} \times \text{cm}^{-2}$	1.48 ± 0.04	0.74 ± 0.02
Bulk: Model B2	$U_O, S \times \text{cm}^{-1}$	2.0 ± 0.5	1.2 ± 0.5
Permeate: Model S3	$J_1^0, \mu\text{mol} \times \text{s}^{-1} \times \text{cm}^{-2}$	0.8 ± 0.2	0.4 ± 0.2
	R_{adj}	0.9993	0.9990
Feed: Model S1	$J_2^0, \mu\text{mol} \times \text{s}^{-1} \times \text{cm}^{-2}$	1.59 ± 0.07	0.77 ± 0.01
Bulk: Model B3	$U_O, S \times \text{cm}^{-1}$	110 ± 20	30 ± 10
Permeate: Model S3	$J_1^0, \mu\text{mol} \times \text{s}^{-1} \times \text{cm}^{-2}$	0.7 ± 0.1	0.3 ± 0.1
	R_{adj}	0.9992	0.9994

* For Model B3, $n=10$; for Models S1 and S2, $z=2$ and $f(c_{\text{lim}})=\delta$ and 1, respectively (see text). The indices “1” and “2” correspond to the permeate- and feed-side surfaces, respectively

Conclusions

The incorporation of Sr²⁺ cations and creation of A-site deficiency in La_{1-x-y}Sr_xCoO_{3-δ}, resulting in higher oxygen nonstoichiometry and tendency to defect association, increases the lattice expansion, oxygen ionic conductivity, oxygen permeability of the dense ceramic membranes, and surface exchange limitations, while the stability to reduction and electronic transport in air above 980 K both decrease. In contrast to most ferrite materials, the Mössbauer spectroscopy analysis of La_{1-x}Sr_xCo_{0.99}⁵⁷Fe_{0.01}O_{3-δ} suggests that when the oxygen content is close to stoichiometric, Fe⁴⁺ retains a delocalized electronic state down to 4 K. At oxygen partial pressures higher than 10⁻⁵ atm, no long-range ordering was observed for the compositions with $x = 0.3$ – 0.5 , while the transition into vacancy-ordered tetragonal phase was observed for La_{0.3}Sr_{0.7}Co_{0.99}Fe_{0.01}O_{3-δ} sample annealed at 1223 K in argon atmosphere. Therefore, the $p(\text{O}_2)$ - T - δ diagrams were adequately described by a statistical thermodynamic model combining the rigid-band approach for delocalized holes and the pair-cluster formation reaction involving oxygen vacancies and Co²⁺ cations. Any attempt to complicate this model did not lead to better fitting results. The resultant relationships between the oxygen chemical potential and mobile vacancy concentration were used for numerical regression analysis of the steady-state oxygen permeation through dense La_{1-x}Sr_xCoO_{3-δ} membranes. The oxygen permeability of the La_{0.3}Sr_{0.7}CoO_{3-δ} membranes is governed by surface exchange limitations at both feed and permeate sides. The permeation of La_{0.7}Sr_{0.3}CoO_{3-δ} is limited by the bulk ionic transport. For La_{0.5}Sr_{0.5}CoO_{3-δ} where the roles of both factors are significant, the surface oxygen exchange limitations occurred at the membrane permeate side only. Reducing both $p(\text{O}_2)$ and temperature leads to greater surface limitations. The calculated ionic conductivity is found proportional to the concentration of mobile oxygen vacancies and occupied oxygen sites.

Supplementary information The online version contains supplementary material available at <https://doi.org/10.1007/s10008-021-05023-8>.

Acknowledgements Important experimental contribution and helpful discussions made by I. Marozau are gratefully acknowledged.

Funding The work of ISSP RAS team centered on the synthesis and electrochemical measurements was supported by the Russian Science Foundation (grant 20–19–00478). E.N. Naumovich received financial support from the Ministry of Science and Higher Education of the Republic of Poland for Statutory Grant CPE/001/STAT/20 in the Institute of Power Engineering. A.A. Yaremchenko and A.V. Kovalevsky received financial support within the project CICECO—Aveiro Institute of Materials (UIDB/50011/2020 and UIDP/50011/2020) financed by national funds through the FCT/MCTES and when appropriate co-financed by FEDER under the PT2020 Partnership Agreement. J.C. Waerenborgh also received support from the FCT (Portugal) under the contract UID/Multi/04349/2013.

References

1. Elcogen solid oxide cells and stacks. <https://elcogen.com/products/solid-oxide-fuel-cells>. Accessed 23 June 2021
2. Mougín J, Di Iorio S, Chatroux A, Donnier-Marechal T, Palcoux G, Petitjean M, Roux G (2017) ECS Trans 78:3065–3075
3. Sun X, Sudireddy BR, Tong X, Chen M, Brodersen K, Hauch A (2019) ECS Trans 91:2631–2639
4. Mizusaki J (1992) Solid State Ion 52:79–91
5. Teraoka Y, Nobunaga T, Okamoto K, Miura N, Yamazoe N (1991) Solid State Ion 48:207–212
6. van Doorn RHE, Fullarton IC, de Souza RA, Kilner JA, Bouwmeester HJM, Burggraaf AJ (1997) Solid State Ion 96:1–7
7. Lankhorst MHR, Bouwmeester HJM, Verweij H (1997) J Solid State Chem 133:555–567
8. Søgård M, Hendriksen PV, Mogensen M, Poulsen FW, Skou E (2006) Solid State Ion 177:3285–3296
9. Kharton VV, Tsipis EV, Yaremchenko AA, Marozau IP, Viskup AP, Frade JR, Naumovich EN (2006) Mater Sci Eng B 134:80–88
10. Tsipis EV, Kharton VV (2008) J Solid State Electrochem 12:1367–1391
11. Bucher E, Sitte W, Romb I, Papst I, Grogger W, Hofer F (2002) Solid State Ion 152–153:417–421
12. Patrakeeve MV, Leonidov IA, Mitberg EB, Lakhtin AA, Vasiliev VG, Kozhevnikov VL, Poeppelmeier KR (1999) Ionics 5:444–448
13. Chen CH, Bouwmeester HJM, van Doorn RHE, Kruidhof H, Burggraaf AJ (1997) Solid State Ion 98:7–13
14. Tsipis EV, Naumovich EN, Patrakeeve MV, Yaremchenko AA, Marozau IP, Kovalevsky AV, Waerenborgh JC, Kharton VV (2011) Solid State Ion 192:42–48
15. Kovalevsky AV, Kharton VV, Tikhonovich VN, Naumovich EN, Tonoyan AA, Reut OP, Boginsky LS (1998) Mater Sci Eng B 52:105–116
16. Kharton VV, Kovalevsky AV, Yaremchenko AA, Figueiredo FM, Naumovich EN, Shaulo AL, Marques FMB (2002) J Membrane Sci 195:277–287
17. Kozhevnikov VL, Leonidov IA, Mitberg EB, Patrakeeve MV, Petrov AN, Poeppelmeier KR (2003) J Solid State Chem 172:296–304
18. Parkash O, Ganguly P, Rao GR, Rao CNR, Rajoria DS, Bhide VG (1974) Mater Res Bull 9:1173–1176
19. Russo N, Furfori S, Fino D, Saracco G, Specchia V (2008) Appl Catal B: Environ 83(1–2):85–95
20. Lee HN, Jeon H, Choi WS, Biegalski M, Folkman ChM, Tung I-Ch, Fong DD, Freeland JW, Shin D, Ohta H, Chisholm MF (2017) US patent 9550166 B2
21. Petrov AN, Cherepanov VA, Zuev A (2006) J Solid State Electrochem 10:517–537
22. Kharton VV, Kovalevsky AV, Patrakeeve MV, Tsipis EV, Viskup AP, Kolotygin VA, Yaremchenko AA, Shaula AL, Kiselev EA, Waerenborgh JC (2008) Chem Mater 20:6457–6467
23. Waerenborgh JC, Rojas DP, Vyshatko NP, Shaula AL, Kharton VV, Marozau IP, Naumovich EN (2003) Mater Lett 57:4388–4393
24. Kharton VV, Waerenborgh JC, Viskup AP, Yakovlev S, Patrakeeve MV, Gaczyński P, Marozau IP, Yaremchenko AA, Shaula AL, Samakhval VV (2006) J Solid State Chem 179:1273–1284
25. Kharton VV, Patrakeeve MV, Waerenborgh JC, Kovalevsky AV, Pivak YV, Gaczyński P, Markov AA, Yaremchenko AA (2007) J Phys Chem Solids 68:355–366
26. Klencsár Z, Kuzmann E, Vértes A (1996) J Radioanal Nucl Chem 210:105–118
27. Németh Z, Klencsár Z, Kuzmann E, Homonnay Z, Vértes A, Grenèche JM, Lackner B, Kellner K, Gritzner G, Hák J, Vad K, Mészáros S, Kerekes L (2005) Eur Phys J B 43:297–303

28. Shinjo T, Takano M, Taguchi H, Shimada M (1980) *J Phys Colloques* 41:C1–157–C1–158
29. Kawasaki S, Takano M, Takeda Y (1996) *J Solid State Chem* 121:174–180
30. Dann SE, Currie DB, Weller MT, Thomas MF, Al-Rawwas AD (1994) *J Solid State Chem* 109:134–144
31. Adler P, Lebon A, Damljanić V, Ulrich C, Bernhard C, Boris AV, Maljuk A, Lin CT, Keimer B (2006) *Phys Rev B* 73:094451
32. Battle PD, Gibb TC, Nixon S (1988) *J Solid State Chem* 77:124–131
33. Kawasaki S, Takano M, Takeda Y (1998) *Solid State Ion* 108:221–226
34. Gspan C, Grogger W, Bitschnau B, Bucher E, Sitte W, Hofer F (2008) *J Solid State Chem* 181:2976–2982
35. Istomin S, Drozhzhin OA, Svensson G, Antipov EV (2004) *Solid State Sci* 6:539–546
36. Mastin J, Einarsrud M-A, Grande T (2006) *Chem Mater* 18:6047–6053
37. Lein HL, Wiik K, Grande T (2006) *Solid State Ion* 177:1795–1798
38. Hayashi H, Suzuki M, Inaba H (2000) *Solid State Ion* 128:131–139
39. De Groot SR, Mazur P (1984) *Nonequilibrium Thermodynamics*. Dover, New York
40. Adler SB, Chen XY, Wilson JR (2007) *J Catal* 245:91–109

Publisher's Note Springer Nature remains neutral with regard to jurisdictional claims in published maps and institutional affiliations.